# Lawrence Berkeley National Laboratory

Title

Field Quality of HD3—A Nb$_3$Sn Dipole Magnet Based on Block Design

Permalink

https://escholarship.org/uc/item/7qc1f9j0

Journal

IEEE Transactions on Applied Superconductivity, 29(5)

ISSN

1051-8223

Authors

Wang, Xiaorong
Cheng, Daniel W
Dietderich, Daniel R
et al.

Publication Date

2019

DOI

10.1109/tasc.2019.2897138

Peer reviewed

# Field quality of HD3 – a Nb₃Sn dipole magnet based on block design

Xiaorong Wang, Daniel W. Cheng, Daniel R. Dietderich, Joseph DiMarco, Hélène Felice, Paolo Ferracin,
Maxim Marchevsky, Soren O. Prestemon, GianLuca Sabbi

*Abstract*—**HD3 is the latest magnet of a series of block-type Nb₃Sn dipole model magnets developed by the Superconducting Magnet Program at Lawrence Berkeley National Laboratory. The magnet is 1 m long with a clear aperture of 43 mm. As a model magnet designed with accelerator-quality features, each coil has flared ends to provide a clear bore for a beam tube. The magnet design was also optimized to minimize the geometric and saturation field errors. In 2013, HD3b reached a peak dipole field of 13.4 T at 4.4 K. As part of the magnet test, we measured field quality using rotating coils with lengths of 26 mm and 130 mm developed by Fermi National Accelerator Laboratory. Here, we report and analyze the measured static and dynamic field errors. We discuss the insight provided by the field quality study of HD3, which can be useful for the development of high-field block-type dipole magnets for next-generation circular colliders.**

*Index Terms*—**Nb₃Sn dipole magnets, block-type design, field quality.**

## I. Introduction

**T**HE brittle and strain-sensitive Nb₃Sn conductor is currently the conductor of choice for future high-field superconducting accelerator magnets due to its high critical-current density ($J_c$) in the field range of 11 – 16 T and the maturing Nb₃Sn accelerator magnet technology.

In the block design, coils are wound with flat Rutherford cables similar to a racetrack coil with flared ends to provide clearance for the beam path [1]. Compared to the classic $\cos\theta$ design, the block design has several unique features [2]. One can increase the number of turns rather than layers to increase the aperture field. This leads to a more compact magnet configuration with less internal supporting parts. The high-field and high-stress regions are separated, which can reduce the impact of transverse stress on the cable performance.

To develop the block-design magnet technology, the Superconducting Magnet Program at Lawrence Berkeley National Laboratory (LBNL) developed and tested several model dipole magnets (HD series). The magnet had two coils with two layers in each coil and was supported by an aluminum shell-based structure [3], [4]. Following the demonstration of a record 15.4 T in HD1 [5], HD2 introduced the flared coil ends

with a clear aperture of 36 mm [6]–[8] and reached 13.8 T at 4.4 K [9]. Recently, a 100 mm aperture block-type dipole magnet (FRESCA2) reached 13.3 T at 4.3 K [10]–[12] and 14.6 T at 1.9 K [13]. Nb₃Sn block-type dipole magnets were also proposed for future circular colliders [2], [14]–[17].

Although excellent designed field quality was demonstrated [6], [7], [17], there are limited reports on the measured field quality for the block-type dipole magnets [12], [18], [19]. Here, we report the measurement and analysis of the field quality of the HD3b magnet, the latest block magnet developed at LBNL. The HD3b magnet reached a dipole field of 13.4 T at 4.4 K [19]. At 13 T, it demonstrated field errors below 3 units except for $a_2$ and $b_3$ at a reference radius of 13 mm. A warm-cold correlation was also observed. We expect the study to provide useful input for the development of high-field block dipole magnets for next-generation circular colliders.

## II. The HD3b Magnet

HD3b was wound with Rutherford cables based on 0.8 mm diameter rod-restack-process (RRP) [20] Nb₃Sn strands with a subelement diameter ($d_{\text{eff}}$) of about 80 $\mu$m (Table I). Fig. 1 shows the cross sectional view of the top coil in the straight section of HD3b.
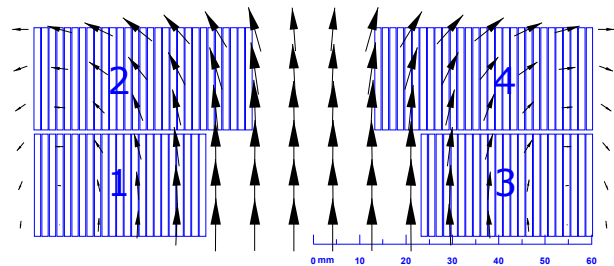


Fig. 1.   The top coil (Coil 3) and field vectors in HD3b magnet plotted by ROXIE [21]. Layer 1 (Blocks 1 and 3) has 23 turns and Layer 2 (Blocks 2 and 4) has 29 turns.

To improve the loading performance and electrical integrity, HD3b implemented several changes with respect to HD2 that affected the optimized field quality. The mid-plane gap between two coils was increased to improve the electrical integrity, which increased the allowed harmonics [22]. To address the clustered quench origins observed in HD2, the radius of the hard-way bend for the flared coil ends was increased from 349 mm in HD2 to 873 mm in HD3, reducing the straight section to about 390 mm [23]. More details on the design, fabrication and test of HD3b magnet can be found in [19], [22], [23].

| Parameter | Unit | Value |
|---|---|---|
| Strand number | - | 51 |
| Core material | - | none |
| Strand diameter before HT | mm | 0.80 |
| Cable pitch length | mm | 130 |
| Filament pitch length | mm | 14 |
| Bare cable width | mm | 22.027 |
| Bare cable thickness | mm | 1.401 |
| Keystone angle | degree | 0 |

## III. MEASUREMENT SETUP, TEST PROTOCOL AND DATA REDUCTION

The field quality was measured with two rotating probes based on the printed circuit board technology developed by Fermi National Accelerator Laboratory [24]. The first probe (PCB2) had two layers of printed circuits and onboard amplifiers for the unbucked and dipole-bucked voltage signals. The second probe (PCB4b) had 10 layers of printed circuits without onboard amplifier. Both probes have two coils with 26 and 130 mm nominal lengths to match the cable pitch length (Table I). The nominal radius for the outer most circuit trace is 11.75 mm to fit into an existing anticryostat with an inner diameter of 25.4 mm.

The PXI-based data acquisition system digitized the probe voltage and encoder signals from each rotation of the probe [18]. To study the impact of flux jumps on the field quality, we digitized the voltage across each layer of the magnet synchronized to the acquisition of the voltage data from the rotating probe.

Scans along the magnet aperture were performed at room temperature before cooldown at $\pm 20$ A with steps of 26 mm. The scans were repeated at 4500 A, 4.4 K. We then measured the static and dynamic field qualities with the 130 mm long coil rotating at the magnetic center with various current ramping profiles at 4.4 K. Typical rotation speed for the probe was 1 Hz.

The magnetic field in the aperture is expressed as a series expansion given by

$$B_y + iB_x = B_1 \times 10^{-4} \sum_{n=1}^{\infty} (b_n + ia_n) \left( \frac{x + iy}{R_{\text{ref}}} \right)^{n-1}, \quad (1)$$

where $b_n$ is the normal and $a_n$ is the skew multipole coefficient of order $n$. They are normalized to the dipole field ($B_1$) and are expressed in units at a reference radius ($R_{\text{ref}}$) of 13 mm [25]. More details of the data reduction can be found in [26].

To study the ramp-rate dependence of the field errors, we define the dynamic multipoles as the difference between the field errors from the continuous ramp and those from the static stair-step measurements. The resulting field errors are then normalized to the static main field [27].

## IV. STATIC FIELD QUALITY

### A. Transfer function and field errors

Figs. 2 and 3 show the measured dipole transfer function and low-order field errors as a function of current. The measurement data were averaged from the up and down ramp branches of the stair-step measurements at 4.4 K. The calculation was based on the as-built magnet geometry (more details below) considering the geometric and iron saturation effects. The persistent-current effects which dominated the field errors below 5 kA was reported in [28].
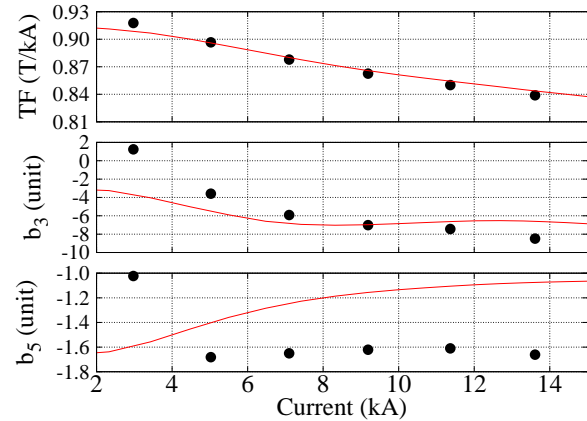
Fig. 2. The dipole transfer function, $b_3$ and $b_5$ as a function of current. Measurements: point. Calculation: line. 4.4 K. $R_{\text{ref}} = 13$ mm.
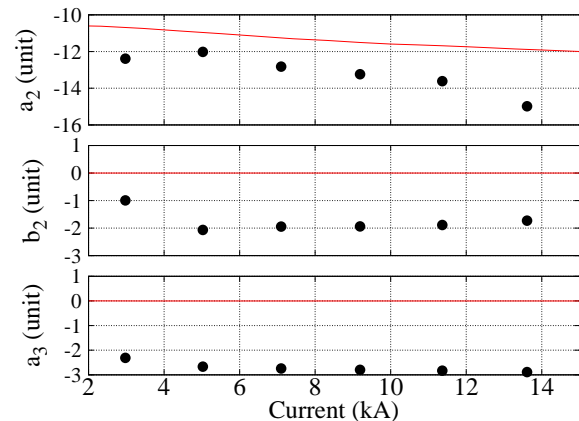
Fig. 3. Low-order non-allowed field errors as a function of current. Measurements: point. Calculation: line. 4.4 K. $R_{\text{ref}} = 13$ mm.

The measured saturation effect generally agreed with the calculation within 2 units except for the main field transfer function that was 0.6% lower than the calculation at 13.6 kA. The non-allowed $b_2$ and $a_3$ showed negligible saturation effect, consistent with the calculation.

Table II compares the measured and calculated field errors at 15.575 kA (13 T aperture field). The harmonics were measured with the 130 mm probe at the magnetic center after holding the current for about 230 s to minimize the dynamic effects. The calculation included the persistent-current effects: 0.7 units for $b_2$ and $-1.5$ units for $b_3$ [28].

The calculated harmonics were based on the following as-built magnet dimensions: 0.762 mm of mid-plane gap with respect to the nominal value of 0.610 mm. According to the insulation shim thickness between the coil and side rails, Layer 1 in Coil 3 is 0.787 mm thinner than Layer 1 in Coil 1. Layer 2

| $n$ | Measurement | | Calculation | |
|---|---|---|---|---|
| | $b_n$ | $a_n$ | $b_n$ | $a_n$ |
| 2 | −1.8 | −14.5 | 0.7 | −12.0 |
| 3 | −9.1 | −2.9 | −8.5 | 0.0 |
| 4 | 0.2 | −0.4 | −0.1 | −1.1 |
| 5 | −1.7 | −0.4 | −1.1 | 0.0 |
| 6 | 0.0 | −0.1 | 0.0 | −0.2 |
| 7 | −1.8 | 0.0 | −1.1 | 0.0 |
| 8 | 0.0 | 0.0 | 0.0 | 0.0 |
| 9 | −1.2 | 0.1 | −0.9 | 0.0 |
| 10 | 0.0 | 0.0 | 0.0 | 0.0 |

in Coil 3 is 0.635 mm thinner than Layer 2 in Coil 1. Moving the coil pack by −0.6 mm along the mid-plane inside the iron yoke can reproduce the measured $b_2$ component.

Fig. 4 compares the measured and calculated profiles of the transfer function and $b_3$ along the magnet aperture measured at 4.5 kA (up ramp) using the 26 mm long probe. Over one coil end ($z$ between 200 and 500 mm), the integrated $b_3$ was −47 unit-m and the integrated $b_5$ was −3 unit-m.
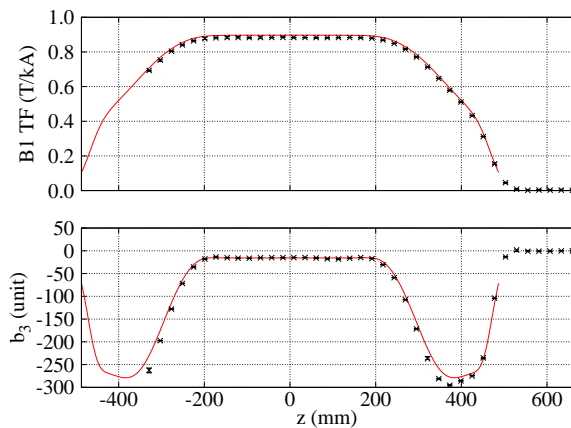


Fig. 4.  Harmonic profiles along the magnet aperture at 4.5 kA (up ramp) using the 26 mm long probe. Measurements: cross. Calculation: line. The $b_3$ calculation was shifted by −15 units. 4.4 K. $R_{\mathrm{ref}} = 13$ mm.

Fig. 5 shows a zoomed-in profile of $b_3$ in the straight section, together with the data measured at 290 K with the 26 mm long probe.

To estimate the variance of coil block positioning along the magnet aperture, we fit the standard deviation of the field errors [$\sigma(a_n, b_n)$] measured at eight locations within ±100 mm around the magnetic center ($z = 0$). Fig. 6 plots the $\sigma(a_n, b_n)$ as a function of harmonic order. The plateau beyond $n = 6$ indicated a probe resolution of 0.1 unit at the probe radius (11.75 mm). By fitting the data with the scaling law on the field errors due to random coil block displacement [29], [30], we determined the variance of the coil block positioning along the magnet aperture was 26 $\mu$m rms for HD3b.

### B. Warm-cold correlation

Fig. 7 plots the warm-cold correlation between the field errors. The cold data were from Table II. We labeled the
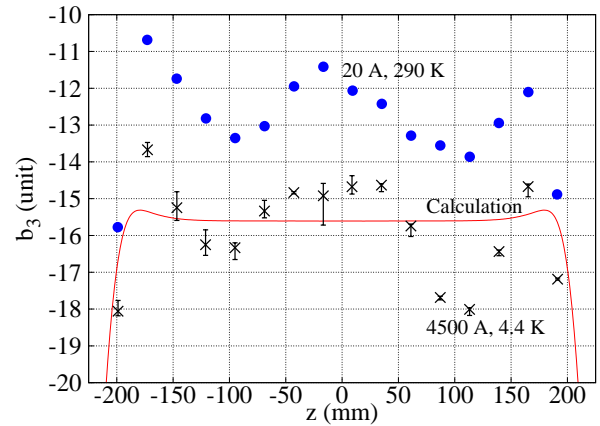


Fig. 5.  Comparison between the $b_3$ profiles measured at 20 A, 290 K and 4500 A, 4.4 K. The calculated $b_3$ calculation was shifted by −15 units. $R_{\mathrm{ref}} = 13$ mm.
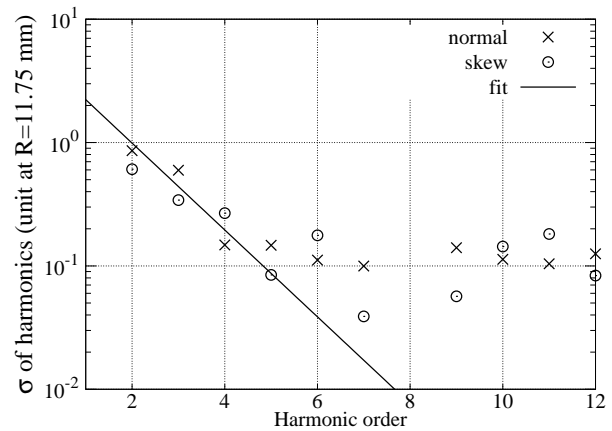


Fig. 6.  The standard deviation of the harmonics indicate a 26 $\mu$m rms positioning error along the magnet aperture. $R_{\mathrm{ref}} = 11.75$ mm.

field errors that deviate from the line with a unit slope which corresponds to a 1 to 1 correlation.
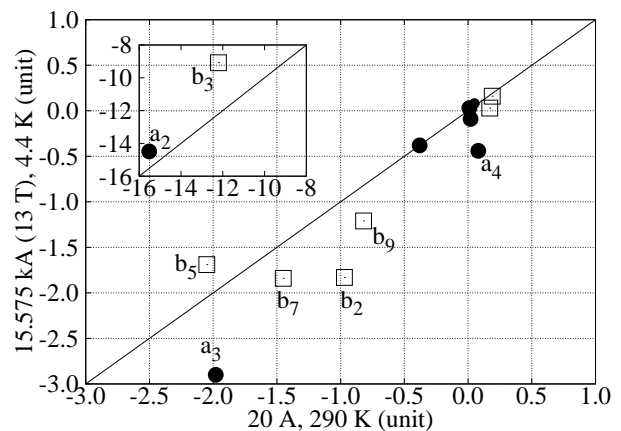


Fig. 7.  Correlation between the harmonics up to $n = 9$ measured at 290 K, ±20 A and 4.4 K, 15.575 kA (13 T dipole field). The inset shows $a_2$ and $b_3$ with large amplitudes. $R_{\mathrm{ref}} = 13$ mm.

To quantify the warm-cold correlation with respect to the unit slope, we used the difference between the warm and

cold harmonics. For instance, the deviation of warm-cold correlation of harmonics $b_n$ from the unit slope is given by $d(b_n) = |b_{n,\text{warm}} - b_{n,\text{cold}}|$. Smaller $d(b_n)$ means a stronger warm-cold correlation. Table III gives the $d(b_n)$ and $d(a_n)$ for Fig. 7.

TABLE III
THE DIFFERENCE ($d$) BETWEEN THE WARM AND COLD HARMONICS.
$R_{\text{REF}} = 13$ MM.

| $n$ | $d(b_n)$ | $d(a_n)$ |
|-----|----------|----------|
| 2   | 0.9      | 1.0      |
| 3   | 3.1      | 0.9      |
| 4   | 0.0      | 0.5      |
| 5   | 0.4      | 0.0      |
| 6   | 0.1      | 0.1      |
| 7   | 0.4      | 0.0      |
| 8   | 0.0      | 0.0      |
| 9   | 0.4      | 0.0      |
| 10  | 0.2      | 0.0      |

## V. DYNAMIC BEHAVIOR

### A. Ramp-rate dependence caused by the low cross-contact resistance in Rutherford cables

Strong decay of the main field and field errors were observed when the ramp rate of the current changed [19]. For instance, the main field transfer function decayed for about 42 units when the ramp rate reduced from 20 to 0 A/s at 11.3 kA (Fig. 8). An exponential fit with a single time constant ranging from 30 to 64 s can describe most field errors except for $b_2$ and $a_3$.
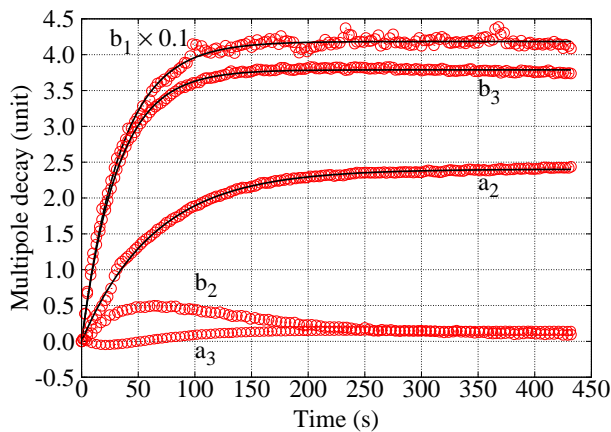


Fig. 8. Decay of the normalized main field transfer function ($b_1$) and low-order multipoles at 11.3 kA (9.6 T aperture field), 4.4 K. The ramp rate reduced from 20 A/s to 0 at time 0. The data were shifted to a common reference at time 0. Open circles: measurement. Solid lines: exponential fit. $R_{\text{ref}} = 13$ mm.

The decay amplitude of the field errors scaled with ramp rates. Fig. 9 shows an example measured during the up ramp at 9.1 kA, 4.4 K. The decay amplitudes were normalized to the static main field at 9.1 kA.

We attributed the exponential decay and the ramp-rate dependence of the decay amplitude to the inter-strand coupling currents in the non-cored Rutherford cables. To estimate the cross contact resistance ($R_c$), we followed the analysis
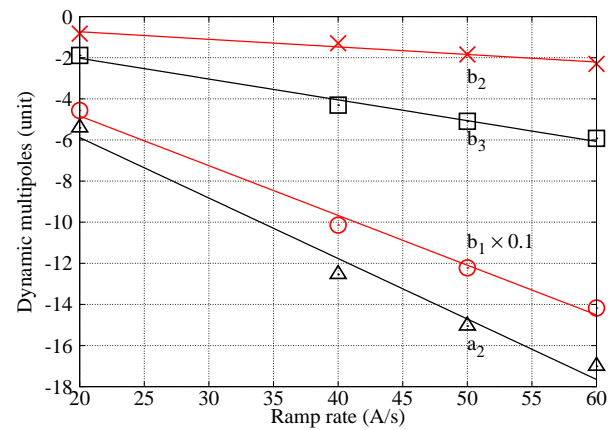


Fig. 9. Measured low-order dynamic multipoles as a function of ramp rates at 9.1 kA, 4.4 K. Solid lines are the least-square linear fit of the measured multipoles. $R_{\text{ref}} = 13$ mm.

approach used for earlier NbTi and Nb$_3$Sn magnets [27], [31]–[33] to correlate the measured dynamic field errors and the $R_c$ through the sensitivity matrix as determined by the network approach [31].

Fig. 10 shows the $B_1$ and $B_2$ caused by the inter-strand coupling currents per unit cross contact conductance ($G_c = R_c^{-1}$) from each cable turn in one coil.
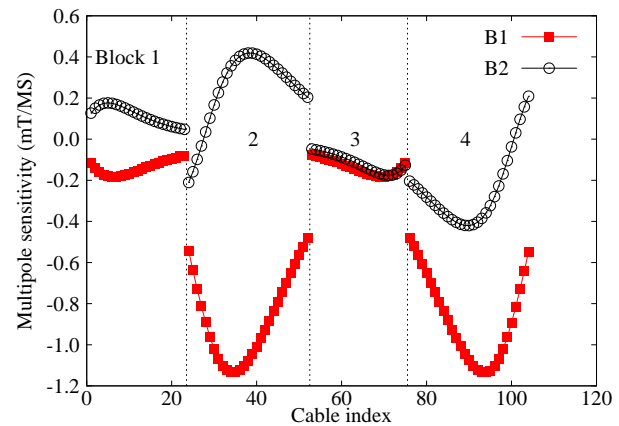


Fig. 10. $G_c$ sensitivity of $B_1$ and $B_2$ from each individual turn in one coil (Fig. 1) at 9.1 kA with a ramp rate of 40 A/s, 4.4 K. $R_{\text{ref}} = 13$ mm.

Summing the contribution from individual cables, one obtains the sensitivity of dynamic multipoles for unit $R_c$ uniform across the entire magnet cross section (Fig. 11).

The measured dynamic $B_1$ (Fig. 9) corresponded to an $R_c$ of 1.4 $\mu\Omega$ over all cable turns according to Fig. 11. The measured dynamic $B_3$ gave an $R_c$ of 0.1 $\mu\Omega$ across the magnet cross section. Although this indicated the possible range of $R_c$, uniform $R_c$ across the magnet cross section cannot explain all the measured multipoles. One would need a negative $R_c$ to explain the measured $A_2$ with a uniform $R_c$. This suggested that $R_c$ varied between cable turns.

A quadratic programming approach was used to determine possible $R_c$ distribution to explain the measured multipoles [27], [32], [33]. Fig. 12 shows the $R_c$ distribution that reproduced the measured dynamic field errors, $B_1$, $B_2$, $B_3$ and
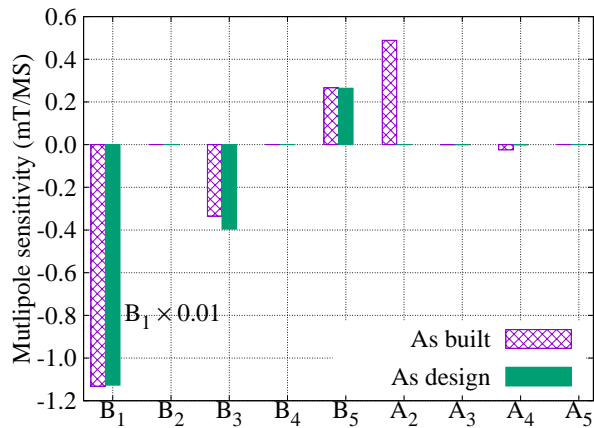
Fig. 11.  $G_c$ sensitivity with uniform $R_c$ across the magnet cross section at 9.1 kA with a ramp rate of 40 A/s, 4.4 K. $R_{ref} = 13$ mm.

$A_2$, at 9.1 kA and 40 A/s, within 0.5%. Both layers in Coil 1 had similar averaged $R_c$ around 1.2 $\mu\Omega$. Layer 2 in Coil 3 had an average $R_c$ higher than that of Layer 1 (Table IV).
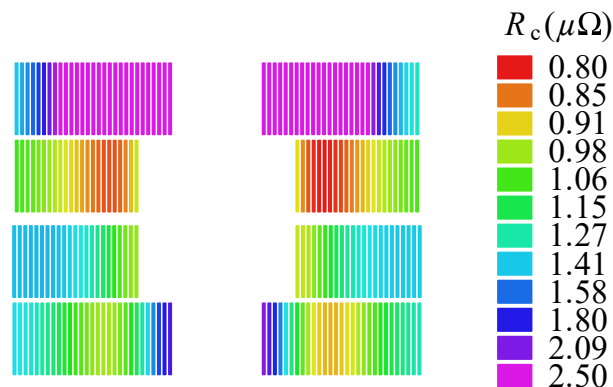


Fig. 12.  $R_c$ in each cable that reproduced within 0.5% the measured $B_1, B_2, B_3$ and $A_2$ at 9.1 kA with a ramp rate of 40 A/s, 4.4 K. To be consistent with the estimation based on the uniform $R_c$, the upper bound for the $R_c$ was set to 2.5 $\mu\Omega$ for the analysis. The top coil is Coil 3.

TABLE IV
THE MEAN AND STANDARD DEVIATION OF THE $R_c$ ($\mu\Omega$) IN EACH COIL AS SHOWN IN FIG. 12.

|  | Mean | Standard deviation |
|---|---|---|
| Coil 1 Layer 1 | 1.3 | 0.2 |
| Layer 2 | 1.2 | 0.3 |
| Coil 3 Layer 1 | 0.9 | 0.1 |
| Layer 2 | 2.3 | 0.4 |

*B. Field errors associated with flux jumps*

As reported in [19], HD3b showed strong fluctuation of field errors associated with flux jumps in Nb$_3$Sn conductors at 4.4 K. The fluctuation featured a change of the field errors on the order of $1 - 10$ units and a decay with a time constant of a few seconds (Fig. 13).

When large fluctuation of field errors occurred at 4.4 K, we observed that current power supply responded to the flux jump
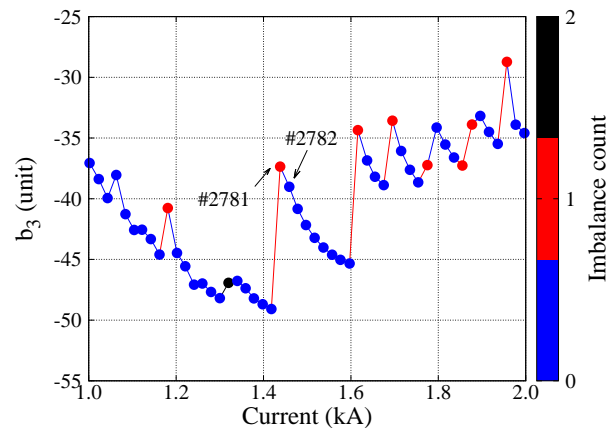


Fig. 13.  Fluctuation of $b_3$ during the up ramp at 20 A/s, 4.4 K. The color code indicates the number of flux jumps detected during each probe rotation. $R_{ref} = 13$ mm.

event. Fig. 14 showed an example for rotation #2781 when $b_3$ jumped for 13 units. At about 53 ms since the beginning of this rotation, a flux jump occurred (coil voltage in Fig. 14 top), followed by a response in the output voltage of the rotating probe (Fig. 14 middle) and a reduction in the magnet current by 5 A at a rate of 185 A/s (Fig. 14 bottom). The magnet current fluctuation was clear when compared to the current ramping profile in the next rotation with no flux jump (#2782 in Fig. 13).
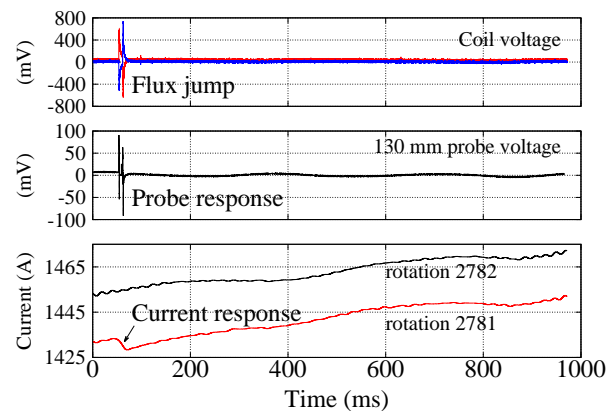


Fig. 14.  Observation during a probe rotation when a flux jump occurred (#2781 in Fig. 13). Top: the flux jump event as indicated by the coil voltage. Middle: the dipole-bucked output voltage of the rotating probe. Bottom: power supply current in rotation #2781 with flux jumps and #2782 without flux jump.

VI. DISCUSSION

HD3b demonstrated good field quality at 13 T, 4.4 K. At a reference radius of 13 mm, 60% or 72% of the clear aperture depending on assembly configuration, the measured field errors were less than 2 units except for $a_2, b_3$ and $a_3$ (Table II). The ROXIE model based on the as-built magnet geometry largely reproduced the observed field errors (Table II): the large allowed terms, in particular $b_3, b_5$ and $b_7$ were due to the increased mid-plane gap [22]; the 14-unit $a_2$ was due to the smaller width of Coil 3 with respect to Coil 1. Reducing

the mid-plane gap and making coils with uniform dimensions can help achieve field errors less than 1 unit as expected from the optimal HD design [6], [7].

HD3b showed large integrated harmonics particularly at the coil ends (Fig. 4). One option to address this issue is to increase the axial distance between the two layers as discussed in [18]. Given that the peak field in the coil end is acceptable, one can also compensate with the harmonics in the magnet straight section. Assuming a magnet with the HD3b coil end design and a 15 m long straight section, one needs +6 units of $b_3$ and +0.4 units of $b_5$ in the straight section to compensate the integrated harmonics at both coil ends. The body-end compensation strategy also allows to keep the compact coil ends.

The variation of $b_3$ along the magnet aperture appears to be related to the conductor positioning, as opposed to persistent currents (Fig. 5). Similar variation of geometric field errors was also observed in the $\cos 2\theta$ LARP HQ [34] and MQXF magnets for the High-Luminosity LHC [35], [36].

Similar to recent Nb$_3$Sn accelerator magnets based on the $\cos n\theta$ design [34], [35], [37], HD3b showed a good warm-cold correlation for the field errors at the magnetic center (Fig. 7). This indicated that the conductor positioning was the main source for the field errors measured in HD3. This geometric effect was not significantly affected by the cooldown and energization. The demonstrated warm-cold correlation can allow effective correction of field errors at room temperature during the magnet assembly stage.

The exponential decay of the multipoles with a single time constant and the ramp-rate dependence of the decay amplitudes suggested strong inter-strand coupling currents (ISCC) in HD3b. This was expected for wind-and-react Nb$_3$Sn Rutherford cables without stainless-steel core [38], [39]. The estimated $R_c$ in HD3b was also consistent with previous Nb$_3$Sn accelerator magnets [27], [40], [41]. Suppressing the ISCC with cored Rutherford cables is necessary to reduce the dynamic field errors and increase the quench currents at high ramp rates as demonstrated in LARP HQ magnets [42].

Reducing geometric errors is also important to reduce the ISCC-induced dynamic field errors, in particular the non-allowed terms. As demonstrated in Figs. 10 and 11, geometric field errors can lead to non-vanishing ISCC-induced terms with uniform $R_c$ for each cable turn. This may explain why the dynamic field errors of non-allowed orders still appear in magnets wound with the cored Rutherford cables [34], [35], [43].

Flux-jump induced fluctuation of field errors was observed in previous Nb$_3$Sn dipole magnets where the conductors had a $d_{eff}$ between 90 and 190 $\mu$m [44] and Nb$_3$Sn quadrupole magnets with $d_{eff}$ between 50 and 70 $\mu$m [34], [45]. At 4.4 K, the amplitude of flux jumps can be high enough to cause the transient fluctuations in power supply output which, in the case of non-cored Rutherford cables, can excite ISCC that lead to the multipole decay following the flux jumps (Figs. 13 and 14). At 1.9 K, flux jumps occur more frequently but with smaller amplitudes [46], which lead to less pronounced fluctuations in field errors [34]. Hence, operation at 1.9 K, cored Rutherford cables to suppress the ISCC and smaller $d_{eff}$ can reduce the

random fluctuation of field errors associated with flux jumps.

## VII. CONCLUSION

Field quality of HD3, a Nb$_3$Sn block-type dipole magnet, was measured with a printed-circuit-board rotating coil at room temperature and 4.4 K. The measured field errors were less than 2 units except for $a_2$ (−15 units), $b_3$ (−9 units) and $a_3$ (−3 units) at a reference radius of 13 mm. The known magnet dimensions can explain the large $a_2$ and $b_3$. A correlation between the field errors at 13 T, 4.4 K and 20 A, 290 K was observed with the difference between the warm and cold harmonics below 1 unit except for $b_3$. The warm-cold correlation indicated that the field errors were largely due to the conductor positioning. Ramp-rate dependence of the field errors were also observed and explained with low cross-contact resistance in the Rutherford cables. Cored cables and reduced geometric errors are expected to reduce the dynamic field errors induced by the inter-strand coupling currents. Strong fluctuation of field errors associated with flux jumps was observed. Nb$_3$Sn strands with smaller sub-element diameters, cored cables and operation at 1.9 K can suppress the impact of flux jumps. Although more studies on the field quality optimization and measurements will be required for future block-type magnets in particular with twin apertures [15], [17], the results of HD3 magnet reported here showed that the block-type dipole magnets can achieve excellent field quality that is required for future circular colliders.

## REFERENCES

[1] P. M. McIntyre, W. Shen, and R. M. Scanlan, "Ultra-high-field magnets for future hadron colliders," *IEEE Trans. Appl. Supercond.*, vol. 5, no. 2, pp. 1099–1102, Jun. 1995.

[2] G. Sabbi, L. Bottura, D. W. Cheng et al., "Performance characteristics of Nb$_3$Sn block-coil dipoles for a 100 TeV hadron collider," *IEEE Trans. Appl. Supercond.*, vol. 25, no. 3, p. 4001407, Jun. 2015.

[3] S. Caspi, S. Gourlay, R. Hafalia et al., "The use of pressurized bladders for stress control of superconducting magnets," *IEEE Trans. Appl. Supercond.*, vol. 11, no. 1, pp. 2272–2275, Mar. 2001.

[4] P. Ferracin, S. Bartlett, S. Caspi et al., "Mechanical design of HD2, a 15 T Nb$_3$Sn dipole magnet with a 35 mm bore," *IEEE Trans. Appl. Supercond.*, vol. 16, no. 2, pp. 378–381, June 2006.

[5] A. F. Lietzke, S. Bartlett, P. Bish et al., "Test results for HD1, a 16 Tesla Nb$_3$Sn dipole magnet," *IEEE Trans. Appl. Supercond.*, vol. 14, no. 2, pp. 345–348, Jun. 2004.

[6] G. Sabbi, S. Bartlett, S. Caspi et al., "Design of HD2: a 15 Tesla Nb$_3$Sn dipole with a 35 mm bore," *IEEE Trans. Appl. Supercond.*, vol. 15, no. 2, pp. 1128–1131, 2005.

[7] P. Ferracin, S. Caspi, D. W. Cheng et al., "Development of the 15 T Nb$_3$Sn dipole HD2," *IEEE Trans. Appl. Supercond.*, vol. 18, no. 2, pp. 277–280, Jun. 2008.

[8] P. Ferracin, B. Bingham, S. Caspi et al., "Recent test results of the high field Nb$_3$Sn dipole magnet HD2," *IEEE Trans. Appl. Supercond.*, vol. 20, no. 3, pp. 292–295, June 2010.

[9] P. Ferracin, B. Bingham, S. Caspi et al., "Assembly and test of HD2, a 36 mm bore high field Nb$_3$Sn dipole magnet," *IEEE Trans. Appl. Supercond.*, vol. 19, no. 3, pp. 1240–1243, Jun. 2009.

[10] A. Milanese, M. Devaux, M. Durante et al., "Design of the EuCARD high field model dipole magnet FRESCA2," *IEEE Trans. Appl. Supercond.*, vol. 22, no. 3, p. 4002604, Jun. 2012.

[11] P. Ferracin, M. Devaux, M. Durante *et al.*, "Development of the EuCARD $Nb_3Sn$ dipole magnet FRESCA2," *IEEE Trans. Appl. Supercond.*, vol. 23, no. 3, p. 4002005, Jun. 2013.

[12] G. Willering, C. Petrone, M. Bajko *et al.*, "Cold powering tests and protection studies of the FRESCA2 100 mm bore $Nb_3Sn$ block-coil magnet," *IEEE Trans. Appl. Supercond.*, vol. 28, no. 3, pp. 1–5, Apr. 2018.

[13] G. Willering, M. Bajko, H. Bajas *et al.*, "Performance update of the FRESCA2 100 mm bore $Nb_3Sn$ block coil magnet," 2018, this conference. 1LOr1D-01.

[14] E. Todesco, L. Bottura, G. de Rijk *et al.*, "Dipoles for high-energy LHC," *IEEE Trans. Appl. Supercond.*, vol. 24, no. 3, p. 4004306, June 2014.

[15] G. Sabbi, J. B. Ghini, S. A. Gourlay *et al.*, "Design study of a 16-T block dipole for FCC," *IEEE Trans. Appl. Supercond.*, vol. 26, no. 3, p. 4004705, Apr. 2016.

[16] C. Lorin, D. Durante, and M. Segreti, "EuroCirCol 16 T Block-Coils dipole option for the future circular collider," *IEEE Trans. Appl. Supercond.*, vol. 27, no. 4, pp. 1–5, Jun. 2017.

[17] C. Lorin, M. Segreti, and M. Durante, "Design of a $Nb_3Sn$ 16 T block dipole for the future circular collider," *IEEE Trans. Appl. Supercond.*, vol. 28, no. 3, p. 4005005, Apr. 2018.

[18] X. Wang, S. Caspi, D. Cheng *et al.*, "Magnetic field measurements of HD2, a high field $Nb_3Sn$ dipole magnet," in *Proceedings of PAC*, 2009, p. 283.

[19] M. Marchevsky, S. Caspi, D. Cheng *et al.*, "Test of the high-field $Nb_3Sn$ dipole magnet HD3b," *IEEE Trans. Appl. Supercond.*, vol. 24, no. 3, p. 4002106, June 2014.

[20] J. Parrell, Y. Zhang, M. Field *et al.*, "Internal Tin conductors engineered for fusion and particle accelerator applications," *IEEE Trans. Appl. Supercond.*, vol. 19, no. 3, pp. 2573–2579, 2009.

[21] S. Russenschuck, *Field Computation for Accelerator Magnets: Analytical and Numerical Methods for Electromagnetic Design and Optimization*.    Weinheim: John Wiley & Sons, 2010.

[22] H. Felice, F. Borgnolutti, S. Caspi *et al.*, "Challenges in the support structure design and assembly of HD3, a $Nb_3Sn$ block-type dipole magnet," *IEEE Trans. Appl. Supercond.*, vol. 23, no. 3, p. 4001705, June 2013.

[23] D. Cheng, S. Caspi, D. Dietderich *et al.*, "Design and fabrication experience with $Nb_3Sn$ block-type coils for high field accelerator dipoles," *IEEE Trans. Appl. Supercond.*, vol. 23, no. 3, p. 4002504, June 2013.

[24] J. DiMarco, G. Chlachidze, A. Makulski *et al.*, "Application of PCB and FDM technologies to magnetic measurement probe system development," *IEEE Trans. Appl. Supercond.*, vol. 23, no. 3, p. 9000505, 2013.

[25] A. K. Jain, "Basic theory of magnets," in *CERN Accelerator School: measurement and alignment of accelerator and detector magnets*, 1998, no. CERN-98-05, pp. 1–26.

[26] L. Bottura, "Standard analysis procedures for field quality measurement of the LHC magnets — part I: harmonics," LHC/MTA, Tech. Rep. LHC-MTA-IN-97-007, 2001.

[27] X. Wang, G. Ambrosio, F. Borgnolutti *et al.*, "Multipoles induced by inter-strand coupling currents in LARP $Nb_3Sn$ quadrupoles," *IEEE Trans. Appl. Supercond.*, vol. 24, no. 3, p. 4002607, June 2014.

[28] X. Wang, G. Ambrosio, G. Chlachidze *et al.*, "Validation of finite-element models of persistent-current effects in $Nb_3Sn$ accelerator magnets," *IEEE Trans. Appl. Supercond.*, vol. 25, no. 3, p. 4003006, 2015.

[29] P. Ferracin, W. Scandale, E. Todesco *et al.*, "Modeling of random geometric errors in superconducting magnets with applications to the CERN large hadron collider," *Phys. Rev. ST Accel. Beams*, vol. 3, p. 122403, 2000.

[30] F. Borgnolutti, S. Caspi, P. Ferracin *et al.*, "Reproducibility of the coil positioning in magnet models through magnetic measurements," *IEEE Trans. Appl. Supercond.*, vol. 19, no. 3, pp. 1100–1105, 2009.

[31] A. P. Verweij, "Electrodynamics of superconducting cables in accelerator magnets," Ph.D. dissertation, University of Twente, 1995.

[32] T. Ogitsu, V. Kovachev, and A. Devred, "Influence of inter-strand coupling current on field quality of superconducting accelerator magnets," *Part. Accel.*, vol. 57, pp. 215–235, 1997.

[33] R. Wolf, D. Leroy, D. Richter *et al.*, "Determination of interstrand contact resistance from loss and field measurements in LHC dipole prototypes and correlation with measurements on cable samples," *IEEE Trans. Appl. Supercond.*, vol. 7, no. 2, pp. 797–800, 1997.

[34] J. DiMarco, G. Ambrosio, M. Buehler *et al.*, "Field quality measurements of LARP $Nb_3Sn$ magnet HQ02," *IEEE Trans. Appl. Supercond.*, vol. 24, no. 3, p. 4003905, 2014.

[35] J. DiMarco, G. Ambrosio, G. Chlachidze *et al.*, "Magnetic measurements of the first $Nb_3Sn$ model quadrupole (MQXFS) for the High-Luminosity LHC," *IEEE Trans. Appl. Supercond.*, vol. 27, no. 4, p. 9000105, Jun. 2017.

[36] S. Izquierdo Bermudez, G. Ambrosio, H. Bajas *et al.*, "Geometric field errors of short models for MQXF, the $Nb_3Sn$ low-$\beta$ quadrupole for the high luminosity LHC," *IEEE Trans. Appl. Supercond.*, vol. 28, no. 3, p. 4006306, Apr. 2018.

[37] L. Fiscarelli, S. I. Bermudez, O. Dunkel *et al.*, "Magnetic measurements and analysis of the first 11-T $Nb_3Sn$ 2-in-1 model for HL-LHC," *IEEE Trans. Appl. Supercond.*, vol. 27, no. 4, p. 4002204, Jun. 2017.

[38] J. D. Adam, D. Leroy, L. R. Oberli *et al.*, "Rutherford cables with anisotropic transverse resistance," *IEEE Trans. Appl. Supercond.*, vol. 7, no. 2, pp. 958–961, 1997.

[39] M. Sumption, E. Collings, R. Scanlan *et al.*, "Core-suppressed AC loss and strand-moderated contact resistance in a $Nb_3Sn$ Rutherford cable," *Cryogenics*, vol. 39, no. 1, pp. 1–12, 1999.

[40] A. den Ouden, S. Wessel, E. Krooshoop *et al.*, "Application of $Nb_3Sn$ superconductors in high-field accelerator magnets," *IEEE Trans. Appl. Supercond.*, vol. 7, no. 2, pp. 733–738, 1997.

[41] N. Andreev, G. Apollinari, B. Auchmann *et al.*, "Field quality measurements in a single-aperture 11 T demonstrator dipole for LHC upgrades," *IEEE Trans. Appl. Supercond.*, vol. 23, no. 3, p. 4001804, 2013.

[42] J. DiMarco, G. Ambrosio, M. Anerella *et al.*, "Test results of the LARP $Nb_3Sn$ quadrupole HQ03a," *IEEE Trans. Appl. Supercond.*, vol. 26, no. 4, p. 4005105, June 2016.

[43] L. Fiscarelli, H. Bajas, O. Dunkel *et al.*, "Magnetic measurements on the first CERN-built models of the insertion quadrupole MQXF for HL-LHC," *IEEE Trans. Appl. Supercond.*, vol. 28, no. 3, p. 4002605, Apr. 2018.

[44] A. V. Zlobin, V. V. Kashikhin, and E. Barzi, "Effect of flux jumps in superconductor on $Nb_3Sn$ accelerator magnet performance," *IEEE Trans. Appl. Supercond.*, vol. 16, no. 2, pp. 1308–1311, Jun. 2006.

[45] X. Wang, S. Caspi, D. W. Cheng *et al.*, "Summary of HQ01e magnetic measurements," Lawrence Berkeley National Laboratory, Tech. Rep. LBNL-5290E, 2012.

[46] B. Bordini, D. Richter, P. Alknes *et al.*, "Magnetization measurements of high-$J_c$ $Nb_3Sn$ strands," *IEEE Trans. Appl. Supercond.*, vol. 23, no. 3, p. 7100806, June 2013.